Article

An Analysis of Edge Chipping in $LiTaO_3$ Wafer Grinding Using a Scratch Test and FEA Simulation

Haeseong Hwang, Seungho Han and Hyunseop Lee *

Department of Mechanical Engineering, Dong-A University, Busan 49315, Republic of Korea; 1236157@donga.ac.kr (H.H.); shhan85@dau.ac.kr (S.H.)
* Correspondence: hyunseop@dau.ac.kr

Abstract: Lithium tantalite ($LiTaO_3$) is a representative multifunctional single-crystal material with electro-optical, acoustic, piezoelectric, pyroelectric, and nonlinear optical properties used as a substrate for surface acoustic wave (SAW) devices. To enhance SAW device performance, thinner $LiTaO_3$ substrates with improved surface roughness are desired. Chemical mechanical polishing (CMP) is employed to achieve the desired surface roughness after grinding. However, the thinning process increases the risk of substrate fracture, especially at the edges, resulting in edge chipping. Edge chipping can lead to complete substrate failure during SAW device fabrication, requiring an effective wafer geometry to prevent it. The study utilizes scratch tests and finite element analysis (FEA) to identify the optimal edge shape (C-cut, trimmed, and thinned) for preventing edge chipping on $LiTaO_3$ wafers. The C-cut edge refers to the rounding of the wafer's edge, while the trimmed edge refers to the machining of the wafer's edge to be perpendicular to the wafer surface. As a result of the scratch tests, we observed edge-chipping lengths of 115 and 227 µm on the C-cut and trimmed edges, respectively, while the thinned edge (half C-cut) resulted in complete wafer fracture. In the finite element analysis (FEA), edge-chipping lengths of 80, 120, and 150 µm were obtained on the C-cut, trimmed, and thinned edges (half C-cut), respectively. In conclusion, it has been confirmed that the C-cut, trimmed, and thinned edge shapes are effective in preventing edge chipping. However, considering that the C-cut edge shape becomes thinner through grinding, using the trimmed edge shape appears to be the most effective.

Keywords: edge chipping; finite element analysis (FEA); lithium tantalite ($LiTaO_3$); surface acoustic wave (SAW) device; scratch test

Citation: Hwang, H.; Han, S.; Lee, H. An Analysis of Edge Chipping in $LiTaO_3$ Wafer Grinding Using a Scratch Test and FEA Simulation. *Lubricants* **2023**, *11*, 297. https://doi.org/10.3390/lubricants11070297

Received: 1 June 2023
Revised: 1 July 2023
Accepted: 10 July 2023
Published: 16 July 2023

Copyright: © 2023 by the authors. Licensee MDPI, Basel, Switzerland. This article is an open access article distributed under the terms and conditions of the Creative Commons Attribution (CC BY) license (https://creativecommons.org/licenses/by/4.0/).

1. Introduction

Lithium tantalate ($LiTaO_3$) is a typical multifunctional single-crystal material with electro-optical, acoustic, piezoelectric, pyroelectric, and nonlinear optical properties [1–3]. These properties make $LiTaO_3$ an important functional material for surface acoustic wave (SAW) devices, and thinner processing with a lower surface roughness of $LiTaO_3$ is increasingly required for downsizing and obtaining high-performance products [4–6]. To secure thin thicknesses and high-quality surfaces of $LiTaO_3$, grinding and chemical mechanical polishing (CMP), a process of planarization using a combination of chemical and mechanical forces, are used. However, owing to the brittle nature of $LiTaO_3$, surface defects, such as digs, scratches, dislocations, microcracks, cleavages, subsurface damage, and edge chipping, are observed during the CMP process [7]. Moreover, as the thickness of $LiTaO_3$ becomes thinner, the impact of surface defects on crack nucleation increases, leading to a higher risk of fracture in the $LiTaO_3$ [8]. To identify the cause of the mentioned defects that directly affect the performance of SAW devices, research is being conducted on the mechanical characteristics considered in machining, such as grinding, lapping, and polishing.

Gruber et al. [9] studied cracks in $LiTaO_3$ and lithium niobate ($LiNbO_3$). They conducted a nanoindentation test to determine the direction and length of the cracks through

scanning electron microscope (SEM) image analysis. Consequently, weaker cleavage planes were correlated with the onset of damage, and traces and plastic deformation due to twinning were observed. The results can be generally utilized to evaluate the initiation of damage in other brittle materials and improve the understanding of the damage in anisotropic materials, such as $LiTaO_3$ and $LiNbO_3$. Hang et al. [10] conducted grinding tests via a design of experiment (DOE) analysis, investigating the following parameters: coolant temperature, substrate material, and diamond wheel geometry to clarify the relationship between cracks in $LiTaO_3$ and the effect of temperature during the grinding process. The grinding test results showed that the lower the coolant temperature, the lower the increasing rate of the grinding torque and surface roughness, resulting in fewer cracks, scratches, and breakages. It was also confirmed that the use of a wheel that contributes to effective cooling, such as a heart-type diamond wheel, reduces the occurrence of defects. Wei et al. [11] introduced the underlying mechanisms of material removal in the CMP process of $LiTaO_3$ and conducted scratch and CMP tests. Through the observation and analysis of SEM and acoustic signals obtained from the scratch tests, four regions, namely, elastic regime, plastic regime, plastic regime with cracks, and brittle fracture regime, were observed depending on the force applied to the surface of $LiTaO_3$. Moreover, the addition of H_2O_2 and KOH to the polishing slurry improved material removal and surface roughness in the CMP process. Hang et al. [12] investigate the polishing responses of single-crystal $LiTaO_3$ with three different crystallographic orientations. The investigation of scratch features and friction coefficients was carried out using a nanoindentation system at various velocities. This allowed the determination of nano-hardness values under different strain rates, leading to strain rate sensitivities (SRS) of 0.0172, 0.0455, and 0.043 for the X-112°, Y-42°, and Y-36° planes, respectively. The X-112° plane exhibited better mechanical properties and a "plastic" removal mechanism, resulting in a lower MRR. Moreover, the significantly lower SRS correlated with the relatively lower sensitivity of MRR to rotation speed on the X-112° plane. The findings of this study suggest that the plastic parameter of SRS serves as an excellent indicator for bridging the gap between machining response and intrinsic deformation mechanisms in brittle single-crystal ceramics.

The results of this study showed that factors such as temperature, strain rate sensitivities, force applied to the wafer surface, cutting surface, and cracks affect the surface and internal damage of $LiTaO_3$ during the grinding process. However, the fracture of the $LiTaO_3$ wafer occurs not only on the surface and inside but also at the edges. A typical defect occurring at the edge of a wafer is edge chipping (Figure 1), which is commonly observed in the machining of brittle materials. Owing to grinding, the thickness and strength of the wafer edge are reduced, leading to local damage such as cracks and fractures. This localized damage can then propagate, resulting in wafer breakage. In particular, $LiTaO_3$ has a low fracture toughness, which makes it prone to crack propagation; therefore, research on the conditions for edge chipping is required to prevent damage. Although research on the edge chipping of $LiTaO_3$ wafers remains insufficient, the edge chipping of relatively common silicon wafers has been studied by several researchers.

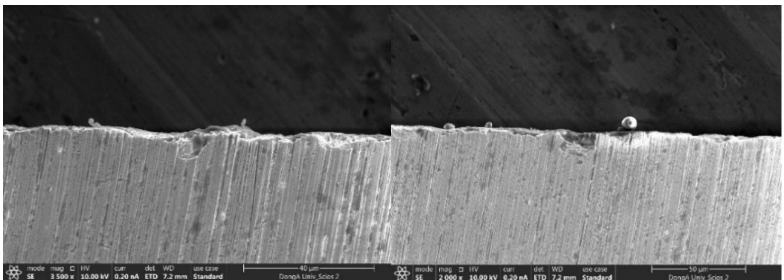

Figure 1. Scanning electron microscope (SEM) images of $LiTaO_3$ edge chipping after grinding (#4000 vitrified grinding wheel, wheel 1400 rpm, chuck 300 rpm, feed rate 0.3 µm/min).

Gao et al. [13] investigated the edge chipping that occurs during the grinding process of silicon wafers and examined the relationship between edge chipping and the grinding conditions, wafer thickness, and crystal orientation of the wafer through grinding experiments. A decrease in the grain size and down-feed rate resulted in a decrease in the edge-chipping size, whereas an increase in the wafer thickness led to an increase in the edge-chipping size. Additionally, the edge-chipping size was larger in the down-grinding mode than in the up-grinding mode. Sun et al. [14] conducted a wafer grinding experiment to experimentally investigate the effect of the wheel and wafer rotation speed, feed rate, and wafer thickness on edge chipping. They observed that the edge-chipping size increased with increasing wafer rotation speed and feed rate but decreased with increasing wheel rotation speed and wafer thickness. Juri et al. [15] investigated the edge-chipping damage in diamond machining of lithium silicate glass-ceramics (LS) and explores the potential of ultrasonic vibration-assisted machining as a solution. The research compares the effects of conventional machining and novel vibration-assisted machining on pre-crystallized and crystallized LS materials. Results show that all edge-chipping damage is caused by brittle fractures, with the extent of damage influenced by material microstructures, mechanical properties, and vibration amplitudes. Pre-crystallized LS exhibits greater damage compared to crystallized LS in conventional machining, but ultrasonic machining at optimized amplitudes significantly reduces the damage. This study highlights the potential of ultrasonic vibration assistance in improving dental CAD/CAM machining techniques by minimizing edge-chipping damage in LS materials. Hirobe et al. [16] introduced numerical analyses for simulating edge chipping caused by impact loading. The authors extend the Particle Discretization Scheme Finite Element Method (PDS-FEM) to simulate fractures resulting from impact loading. The simulations focus on the edge chipping of soda-lime glass using a rigid steel sphere as the impactor while varying the impactor's diameter, impact velocity, and impact distance. The proposed method successfully reproduces the intricate 3D crack patterns observed in edge chipping, such as Hertzian cone cracks and conchoidal chip scars. The method also captures the variations in crack morphology based on the impact force and distance. Additionally, a series of numerical analyses investigate the influence of the impactor's geometry on the dimensions of the chips. The height of the chip remains independent of the impactor's geometry, while the width of the chip depends on it. By demonstrating agreement with experimental results, the study confirms the capability of the proposed method in simulating edge chipping caused by impact loading.

Although the conditions affecting edge chipping in brittle materials, such as silicon and lithium silicate, have been evaluated through grinding experiments, there is a lack of research on edge chipping in $LiTaO_3$. In this study, we aimed to determine the effective edge shape of $LiTaO_3$ wafers to prevent edge chipping during the grinding process of the wafers. We performed scratch tests and finite element analysis (FEA) simulations on wafers with three different edge shapes and analyzed and compared the results to determine the best edge shape among the three.

2. Materials and Methods

2.1. Sample Preparation

The material properties of $LiTaO_3$ used in SAW devices are determined by its atomic arrangement, which is identified by the slicing direction of the $LiTaO_3$ ingot. The distribution of atoms in a plane depends on the slicing direction. Figure 2 and Table 1 illustrate the slicing direction and material properties of the 112° X-cut, 36° Y-cut, and 42° Y-cut $LiTaO_3$ [17,18].

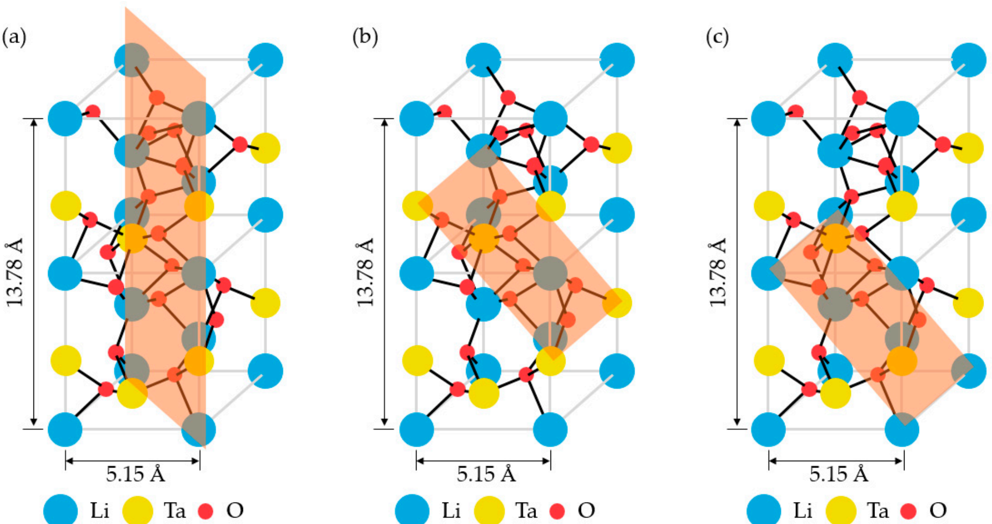

Figure 2. A schematic illustration of the atomic arrangements of single-crystal $LiTaO_3$: (**a**) 112° X-cut; (**b**) 36° Y-cut; (**c**) 42° Y-cut [17,18].

Table 1. SAW velocity, coupling coefficient, and thermal coefficient of delay for three planes [19–22].

Material	SAW Velocity [m/s]	K^2 [%]	TCD [ppm/°C]
112° X-cut $LiTaO_3$	3248	0.75	18
36° Y-cut $LiTaO_3$	4156	6.3	31.5
42° Y-cut $LiTaO_3$	4224	7.8	35

Table 1 summarizes the velocity, coupling coefficient (K^2), and thermal coefficient of delay (TCD) for the 112° X-cut, 36° Y-cut, and 42° Y-cut $LiTaO_3$ shown in Figure 2 [19–22]. K^2 represents the mechanical deformation for electrical input, and TCD refers to the rate of change in the SAW velocity according to temperature variation [19,23]. As K^2 increases, the SAW energy also increases, and a high TCD indicates that the SAW velocity changes significantly with temperature. Upon comparing the material properties of three types of $LiTaO_3$, it was concluded that the 42° Y-cut $LiTaO_3$ exhibited the superior SAW velocity and K^2 among the three types, making it the most suitable for SAW substrate fabrication. Therefore, in this study, 42° Y-cut $LiTaO_3$ with an initial thickness of 200 μm was used for the scratch test.

Edge trimming was performed using an edge grinder (Waferfab, Gunpo-si, Republic of Korea) on a 200-μm thick 4-inch $LiTaO_3$ wafer with a C-cut edge to manufacture a wafer with a vertical edge shape. The C-cut edge refers to the rounding of the wafer's edge, while the trimmed edge refers to the machining of the wafer's edge to be perpendicular to the wafer surface. The machining processes are illustrated in Figure 3, and in this study, the rounding radius of the C-cut was set to 100 μm. For edge grinding, 1200 mesh wheels were used with a wheel rotation speed of 800 rpm and a chuck rotation speed of 2 rpm. To manufacture thinned edge(half C-cut) shape, a 100-μm thick wafer was manufactured by thinning a $LiTaO_3$ wafer with a C-cut edge using a back-grinding machine (DFG830, Disco Corp., Tokyo, Japan). A 4000-mesh vitrified wheel was used for wafer thinning; the rotation speeds of the wheel and the chuck were 1400 rpm and 300 rpm, respectively. After the grinding process, the grinding wheel mark was removed through CMP.

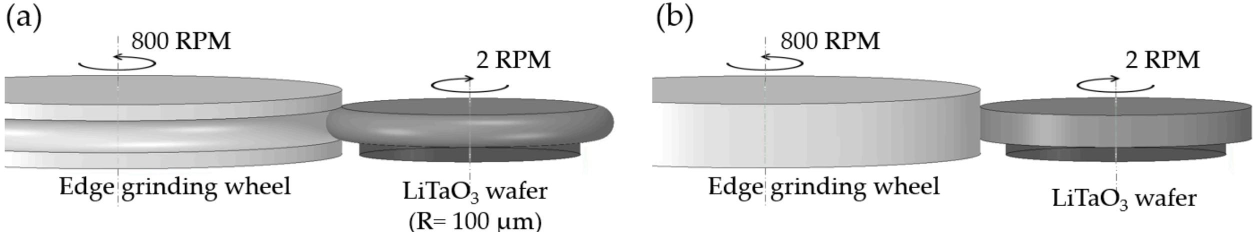

Figure 3. An illustration of $LiTaO_3$ wafer edge grinding: (**a**) C-cut edge; (**b**) Trimmed edge.

2.2. Scratch Test

The scratch tests were conducted at room temperature using a surface scratch tester (JLST022, J&L Tech, Ansan, Republic of Korea), as shown in Figure 4; the test parameters are listed in Table 2. During the scratch test, a Rockwell C diamond cone with a 200-µm radius and a 120-degree cone angle penetrated the $LiTaO_3$ wafers at a constant speed of 0.2 mm/s. The $LiTaO_3$ wafer used in the scratch tests was extremely thin, so breakage or plastic deformation could only occur under the applied normal load of the diamond tip. The test was conducted in two parts: Part 1 to determine the appropriate load to use in the scratch test and Part 2 to apply the determined load and consequently investigate the relationship between edge chipping and edge shape. Part 1 was conducted to determine the load that did not cause breakage or deformation under conditions of 3.0, 4.0, 5.0, and 6.0 N of constant normal force. The determined load was then applied in Part 2, in which scratch tests were performed on three different edge shapes: C-cut, trimmed, and thinned edge (half C-cut). Part 2 aimed to investigate the relationship between edge chipping and edge shape under an applied constant normal force; illustrations of each edge shape are presented in Figure 5.

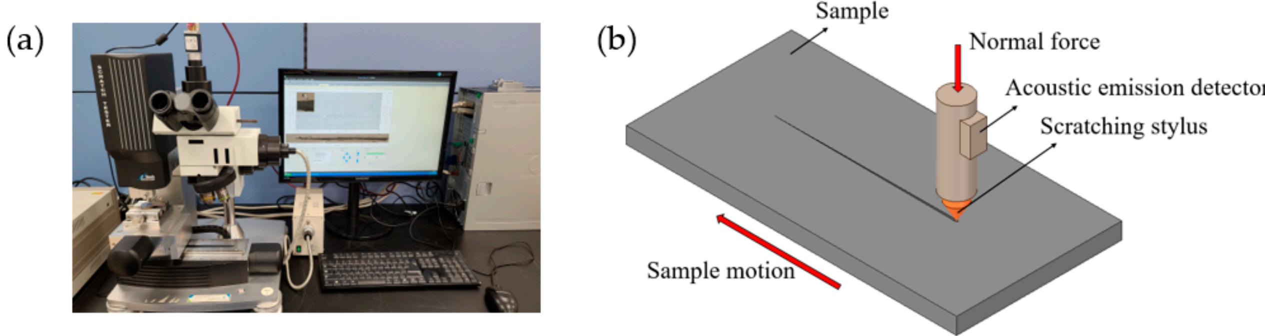

Figure 4. A illustration of the surface scratch tester: (**a**) JLST022, J&L Tech, Ansan, Republic of Korea; (**b**) Measurement principle.

Table 2. The scratch test conditions.

Parameter	Value
Indenter geometry	Conical, 200-µm tip radius, 120-degree cone angle
Scratching speed (mm/s)	0.2
Normal load (N)	3.0 to 6.0
Scratching length (mm)	5 (Part 1) and 10 (Part 2)

Figure 5. A illustration of the $LiTaO_3$ edge shape: (**a**) C-cut edge; (**b**) Trimmed edge; (**c**) Thinned edge (half C-cut edge).

2.3. Finite Element Analysis (FEA)

Finite element analysis (FEA) was used to analytically examine the effect of the edge shape on edge chipping. Figure 6 shows the $LiTaO_3$ geometry used in the simulation, which was modeled to have the same thickness and edge shape as the model used in the scratch test. Finite element models of $LiTaO_3$ wafers with C-cut, trimmed, and thinned edges (half C-cut edge) were generated for the scratch test simulation. The numbers of elements in the generated finite element models were 140,782, 136,383, and 83,191, respectively, and all used tetrahedral elements. The material properties of the diamond indenter and $LiTaO_3$ used for the simulation are presented in Table 3 [9,24–27], and the boundary conditions used for the analysis are listed in Table 4. The scratch test was simulated using ANSYS Transient Structural, a commercial analysis tool. The plastic deformation of the $LiTaO_3$ wafer was observed to evaluate the behavior that occurred when the diamond indenter scratched the surface of the $LiTaO_3$ wafer. The scratch tests conducted in this study can be considered in a quasi-static state with a diamond indenter speed of 0.2 mm/s; therefore, the effects of deformation rate and temperature changes were ignored.

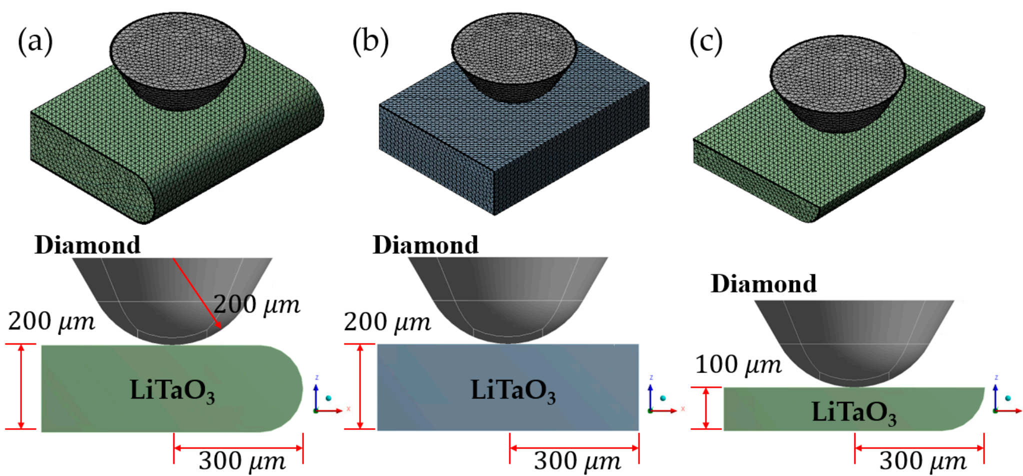

Figure 6. FEA models for three edge shapes of $LiTaO_3$ wafers: (**a**) C-cut edge; (**b**) Trimmed edge; (**c**) Thinned edge (half C-cut edge).

Table 3. Material properties of $LiTaO_3$ for FEA [9,24–27].

Material Properties		Value
$LiTaO_3$	Density (g/mm^3)	7.64
	Young's Modulus (GPa)	248
	Poisson's ratio	0.25
	Yield strength (MPa)	2318
Diamond indenter	Density (g/mm^3)	3.52
	Young's Modulus (GPa)	1220
	Poisson's ratio	0.2

Table 4. Boundary conditions for scratch test simulation.

Boundary Condition	Value
Indenter velocity (mm/s)	0.2
Normal force (N)	4.0
Scratching length (mm)	0.3

3. Results and Discussion

3.1. Scratch Test

3.1.1. Part 1: Scratch Test Regarding Normal Force

Figure 7 shows microscopic images of the surface obtained from the scratch test regarding the constant normal force. The fracture of the $LiTaO_3$ wafer occurred under a load condition of 6.0 N during the scratch test. The black region indicates the area where the fracture occurred, and it begins to appear clear after the indenter has scratched 0.36 mm. The width of the fracture gradually increases from 0.36 to 2.5 mm, and it becomes constant after 2.5 mm. In addition, owing to the brittle nature of $LiTaO_3$, the boundary at which the fracture occurred is rough and irregular. Figure 8 shows the friction force-distance curve obtained from the scratch test regarding the normal force. The average friction forces during scratching were 0.163, 0.343, 1.030, and 2.047 N under constant normal force conditions of 3.0, 4.0, 5.0, and 6.0 N, respectively. Under the constant normal force condition of 6.0 N, the friction force signal began to fluctuate after 0.36 mm, where the fracture of the $LiTaO_3$ wafer started; the cause of the fluctuation is attributed to the rough and uneven boundaries formed around the scratch path. Based on the results of the four different constant normal force conditions, it can be observed that under the 6.0 N constant normal force condition, fracture occurs, making it difficult to observe edge chipping in the experiment with edge shapes. Furthermore, by examining Figure 8, it can be noticed that as the constant normal force increases from 3.0 to 6.0 N, the friction force increases significantly. Specifically, when the constant normal force increases from 3.0 to 4.0 N, the friction force increases by 0.18 N, and when it increases from 4.0 to 5.0 N, the friction force increases by 0.657 N. Moreover, when the constant normal force increases from 5.0 to 6.0 N, the friction force increases by 1.017 N. The friction force under the 5.0 N constant normal force condition shows a sharp increase, approaching the friction force under the 6.0 N constant normal force condition at certain distances (0.5, 1.5, 1.8 mm). Therefore, it was determined that the 5.0 N constant normal force condition is not suitable for the experiment with edge shapes. Consequently, the relatively stable friction force exhibited under the 4.0 N constant normal force was applied in the scratch test regarding edge shapes.

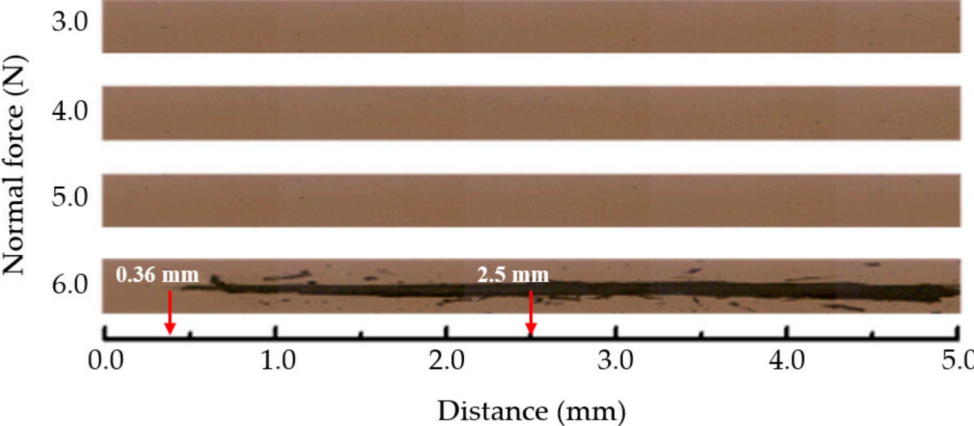

Figure 7. Microscopic images of the surface obtained from the scratch test regarding normal force.

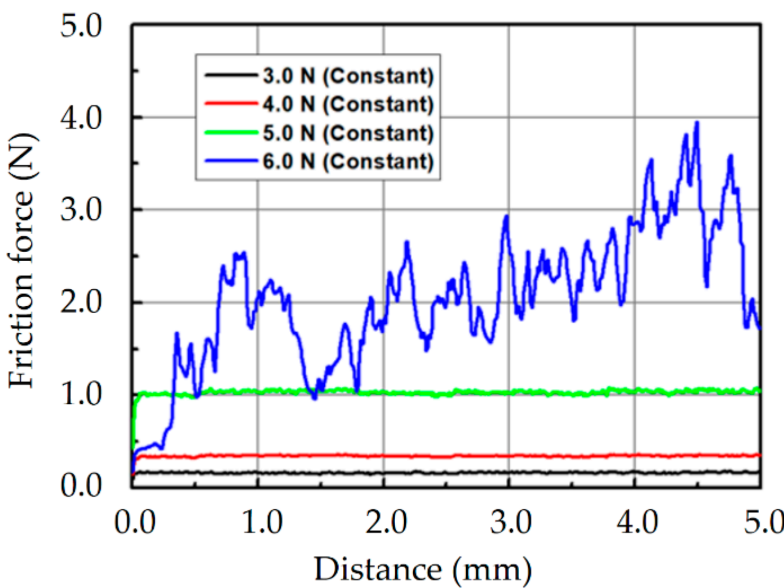

Figure 8. The friction force-distance curve obtained from the scratch test regarding normal force.

In the scratch test regarding normal force, we observed the surface of $LiTaO_3$ at the millimeter scale and measured the friction force. In contrast to the study conducted by He et al. [4], which focused on the micrometer scale, we were unable to determine the exact initiation point of microcrack formation on a microscopic scale. However, it was determined that a normal force of 6.0 N is necessary for the fracture of the $LiTaO_3$ wafer, indicating the threshold for effectively preventing edge chipping. This determination suggests that this value can be considered as a practical normal force to mitigate edge chipping.

3.1.2. Part 2: Scratch Test Regarding Edge Shape

To investigate the relationship between the edge shape and edge chipping, scratch tests were performed on three edge shapes. Three types of edge shapes, namely, C-cut edge, trimmed edge, and thinned edge (half C-cut edge), were used; the thinned edge shape was obtained by machining the C-cut edge wafer. Figure 9 shows the friction force-distance curve and microscopic images of the surface obtained from the scratch test regarding edge shape. The average friction forces for the C-cut, trimmed, and thinned edges were 0.213, 0.253, and 0.809 N, respectively. Additionally, there was a steep drop in the friction force-distance curve, corresponding to the point at which the indenter finished scratching the wafer and detached from it. Qualitative and quantitative evaluation of edge chipping regarding the edge shape was performed by examining microscopic images of the surface. The influence of the edge shape on edge chipping was assessed based on the length of fracture on the wafer edge, resulting in fracture lengths of 115 μm for the C-cut edge and 227 μm for the trimmed edge. For the thinned edge, which had a thinner thickness compared to the C-cut and trimmed edges, a brittle fracture occurred in the $LiTaO_3$ wafer. The rough and discontinuous boundary formed due to the fracture resulted in an increased friction force. The results of the scratch tests demonstrated that the performance of the edge shapes in terms of edge chipping and grinding followed the order of C-cut edge, trimmed edge, and thinned edge, with the C-cut edge showing the best performance. Moreover, there is a requirement to appropriately lower the feed rate due to the risk of fracture in ultrathin wafers.

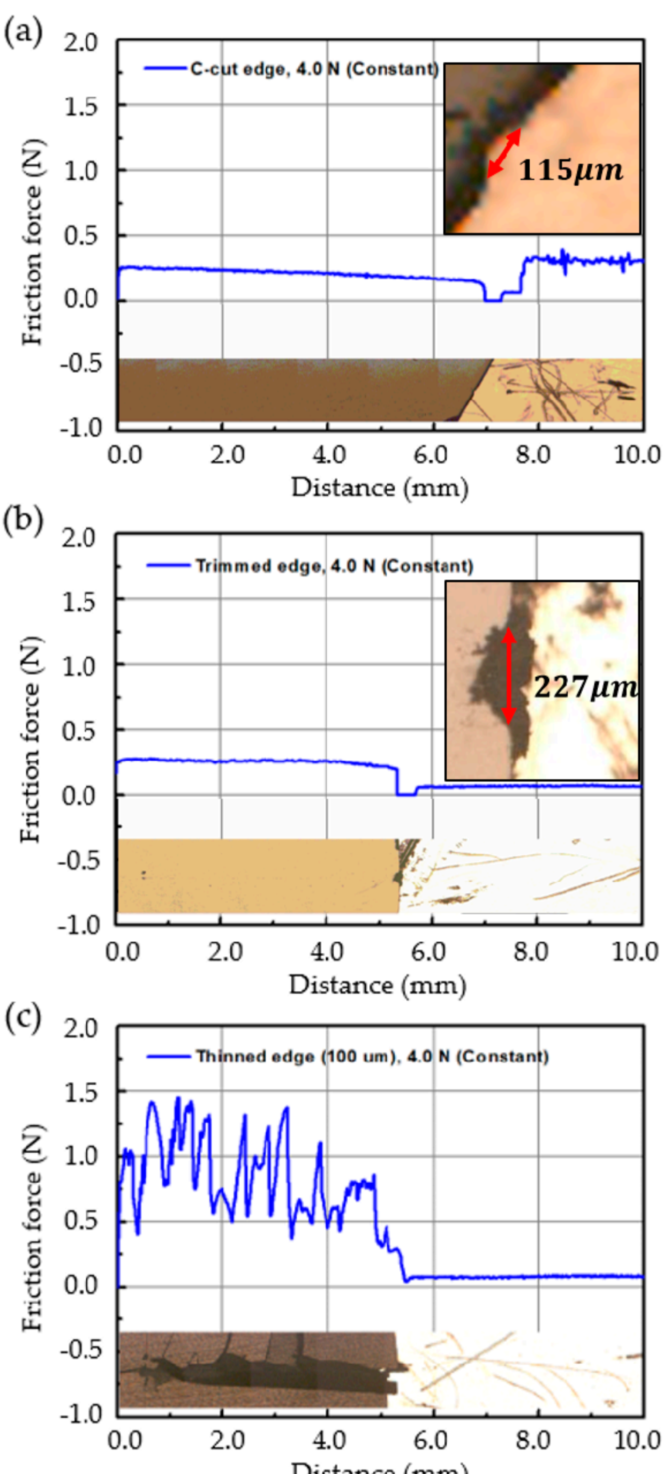

Figure 9. The results of the scratch test regarding edge shape: (**a**) C-cut edge; (**b**) Trimmed edge; (**c**) Thinned edge (half C-cut edge).

This study derived results from the contact between a diamond tip and a $LiTaO_3$ wafer. However, in actual grinding and CMP processes, numerous abrasive particles interact with the wafer, making it necessary to further validate the applicability of the scratch test results to grinding and CMP processes. Therefore, we aimed to validate our results by comparing them with research on silicon wafer edge chipping. In the study by Gao et al. [13], it was argued that during the first half of the wafer thinning process in C-cut edges, the risk of edge chipping is low, but as the wafer thickness decreases, the edges

become sharper, increasing the risk of edge chipping. In the research by Sun et al. [14], a grinding experiment on C-cut wafers was conducted to observe an inverse relationship between thickness and edge-chipping size. These cases align with the trends observed in our study, suggesting that the results obtained from the scratch test can be applied to grinding and CMP processes.

3.2. Finite Element Analysis (FEA)

To perfectly simulate the scratch test conducted previously, a simulation using explicit dynamics would be appropriate. However, it is difficult to use explicit dynamics because the indenter velocity is extremely slow at 0.2 mm/s. Therefore, in this study, the fracture of the $LiTaO_3$ wafer was estimated using ANSYS Transient Structural. Therefore, the fracture of the $LiTaO_3$ wafer was estimated from the plastic deformation obtained from the transient analysis. In scratch tests, the brittle fracture of the $LiTaO_3$ wafer begins after the occurrence of plastic deformation, and because of the nature of brittle materials, it breaks almost immediately when it enters the yielding region beyond the elastic zone. Therefore, the region where plastic deformation occurred was treated as the area where the fracture occurred. Plastic deformation began to occur in the area where the stress exceeded the yield stress of 2318 MPa. During postprocessing, elements, where plastic deformation occurred, were removed and visualized.

Figures 10 and 11 show the deformations of $LiTaO_3$ and von-Mises equivalent stress distributions for the three types of edge shapes obtained from the FEA. The residual-stress region in Figure 11 is the result of plastic deformation caused by the indenter during the scratch test and formed along the scratch path. The maximum deformations observed in the $LiTaO_3$ wafers were 0.0009, 0.0024, and 0.0033 mm for the C-cut, trimmed, and thinned edges, respectively. The maximum stresses observed in the $LiTaO_3$ wafers were 1938, 2136, and 2214 MPa for the C-cut, trimmed, and thinned edges, respectively. The C-cut edge, which is blunter than the trimmed and thinned edges, had the widest contact area with the indenter, resulting in the lowest contact stress. Consequently, it exhibited the smallest deformation and stress among the three edge shapes. However, the largest deformation and greatest stress were observed in the thinned edge. This can be attributed to the deflection caused by an empty space under the edge instead of the $LiTaO_3$ material. In addition, the width of the deformation occurring at the edge was the largest for the thinned edge, which seems to affect the size of the plastic region.

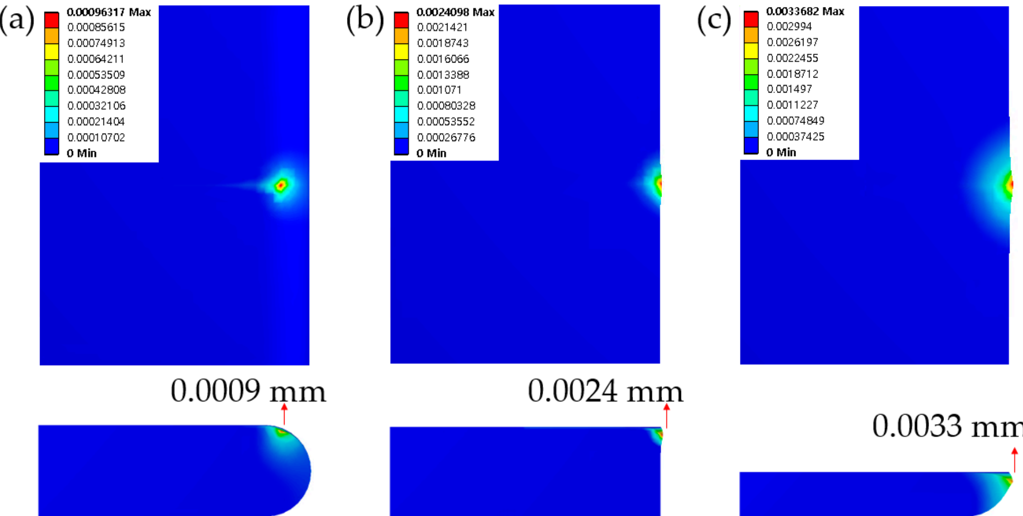

Figure 10. The deformation of $LiTaO_3$ obtained from the scratch test simulation: (**a**) C-cut edge; (**b**) Trimmed edge; (**c**) Thinned edge (half C-cut edge).

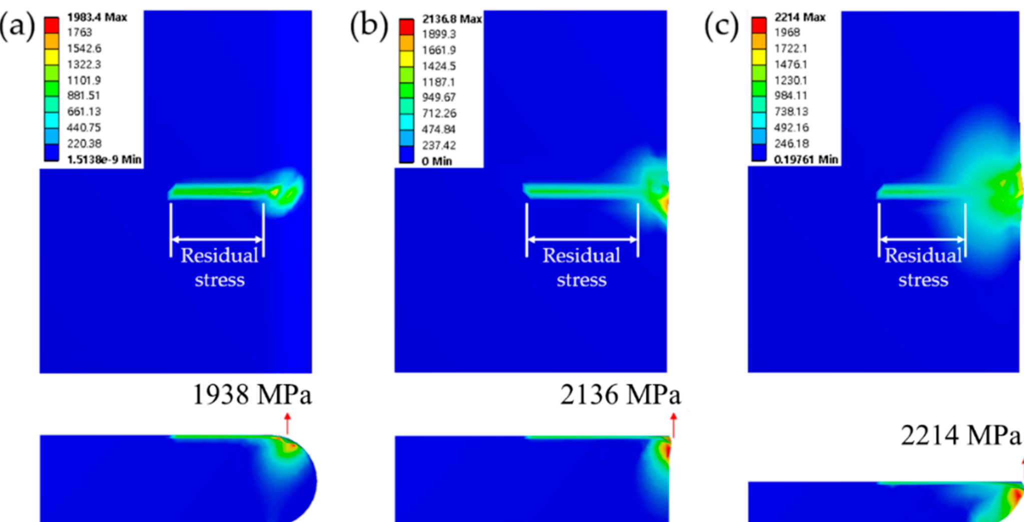

Figure 11. The von-Mises Equivalent stress distribution obtained from the scratch test simulation: (**a**) C-cut edge; (**b**) Trimmed edge; (**c**) Thinned edge (half C-cut edge).

Figure 12 shows the postprocessing of the scratch test simulation results for the three types of edge shapes, focusing on the plastic deformation occurring at the edges. The length of the plastic deformation zone that occurred at the edge of the $LiTaO_3$ wafers with C-cut, trimmed, and thinned edges were 80, 120, and 150 µm, respectively. The results obtained from the transient analysis were consistent with the scratch test results, which confirmed that the C-cut edge shape is superior among the three edge shapes in terms of edge chipping and grinding and that the thinned edge shape shows the largest edge chipping. However, because the C-cut edge shape eventually becomes a thinned edge shape through grinding, there is a risk of fracture or crack occurrence. In manufacturing SAW devices, $LiTaO_3$ is thinned after bonding to a silicon substrate; therefore, the trimmed edge shape among the three edge shapes considered in this study is expected to help reduce edge chipping during grinding. This is expected to improve the quality of the wafer by using a low feed rate.

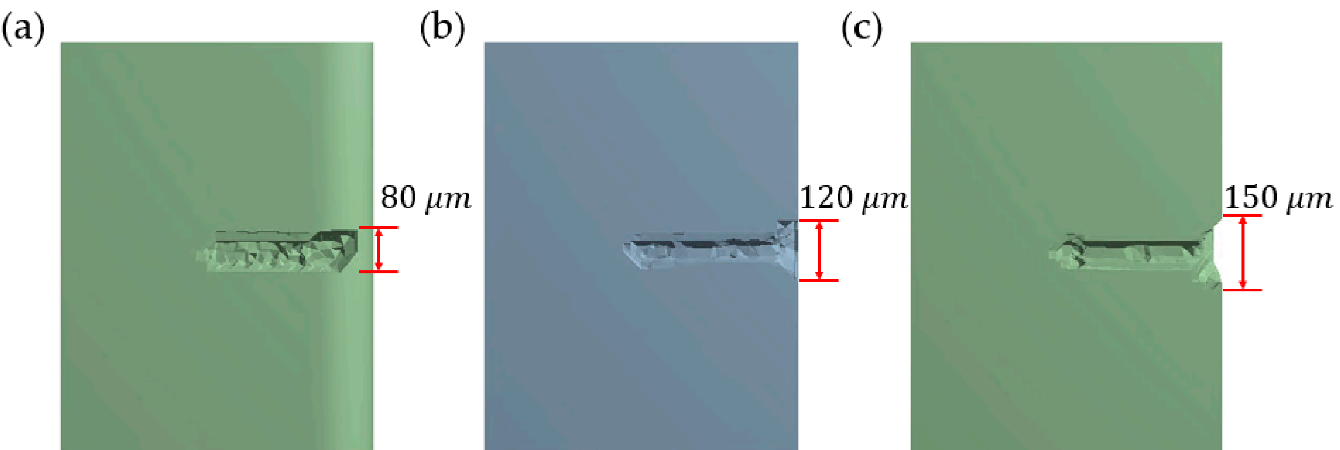

Figure 12. The postprocessing of the scratch test simulation results: (**a**) C-cut edge; (**b**) Trimmed edge; (**c**) Thinned edge (half C-cut edge).

The method of estimating fractures in $LiTaO_3$ wafers during scratch tests through transient structural analysis shows exaggerated results in the surface region, from the start of the scratch test to reaching the edge after the application of normal force when compared

to the results obtained from actual tests. This is because in the stress analysis of the contact surface in transient structural analysis, there are cases where higher stresses occur than the actual physical phenomenon when point contact is made, and it is believed that the higher stress has led to the expansion of the plastic deformation region. On the other hand, the length of edge chipping appeared to be shorter in the transient analysis. This can be attributed to the characteristics of the FEA, which utilizes numerical analyses with a generated mesh. Due to these characteristics, it was not possible to accurately simulate the fracture behavior of $LiTaO_3$, resulting in only plastic deformation occurring at the expected fracture locations and leading to a shorter length of observed edge chipping. However, the optimal shape can be selected through a relative comparison by understanding the tendency of fracture for various shapes of wafers. This method is also expected to apply to other brittle materials, and with further research considering crack and defect mechanisms, a more accurate fracture estimation is possible.

In this study, the transient structural analysis was used as an alternative to the explicit dynamics method for simulating the scratch test to save time and minimize expenses. However, recent research has been actively exploring the application of a method using Smooth-Particle Hydrodynamics (SPH) coupled with the Finite Element Method (FEM) for grinding [28–31]. This method offers the advantages of time efficiency for slow behavior and the ability to simulate realistic behavior. However, the results can vary significantly depending on the number of particles and the setting of the smoothing length, and accuracy may be compromised if an appropriate kernel function is not selected for the analysis model. Nevertheless, existing validated data are based on experiments for simulating grinding analysis using the SPH coupled with the FEM method. By leveraging this data, it is possible to perform grinding analysis for $LiTaO_3$ using the SPH coupled with the FEM method.

4. Conclusions

In this study, scratch tests and finite element analysis (FEA) simulations were performed on wafers with three different edge shapes, and the results were analyzed and compared to determine the best edge shape among the three.

1. Scratch tests regarding the constant normal force applied to the indenter were conducted on the $LiTaO_3$ wafer, and it was confirmed that the wafer fractured at 6.0 N. The constant normal force for the scratch test regarding the edge shape was determined to be 4.0 N.
2. The scratch test results regarding the wafer edge shape enabled a qualitative evaluation of edge chipping, and it was found that the C-cut edge shape was superior among the C-cut, trimmed, and thinned edge (half C-cut) shapes.
3. The effective edge shapes for reducing the edge chipping were determined using the ANSYS Transient Structural. Plastic deformation was used to estimate the fracture of the $LiTaO_3$ wafers, and the results were visualized through postprocessing.
4. Breakage occurred at edges of 80, 120, and 150 μm for the C-cut, trimmed, and thinned edge shapes, respectively. Considering that the C-cut edge shape becomes a thinned edge shape through grinding, the trimmed edge shape was proposed as the most effective edge shape for edge chipping.

Author Contributions: Conceptualization, H.L. and H.H.; methodology, H.L.; validation, H.H., S.H. and H.L.; simulation, H.H.; investigation, H.H. and H.L.; writing—original draft preparation, H.H.; writing—review and editing, S.H. and H.L.; visualization, H.H.; supervision, H.L.; project administration, H.L.; funding acquisition, H.L. All authors have read and agreed to the published version of the manuscript.

Funding: This research was supported by the Nano & Material Technology Development Program through the National Research Foundation of Korea (NRF), funded by the Ministry of Science and ICT (NRF-2022M3H4A3085283).

Data Availability Statement: Not applicable.

Acknowledgments: We would like to thank the Korea Institute of Industrial Technology (KITECH) for allowing us to use the surface scratch tester for this study.

Conflicts of Interest: The authors declare no conflict of interest.

References

1. Oleinik, A.N.; Gilts, M.E.; Karataev, P.V.; Klenin, A.A.; Kubankin, A.S.; Shapovalov, P.G.I.-V. Curve of the Electron Flow Generated during a Pyroelectric Effect in Lithium Tantalate Single Crystal in Vacuum Conditions. *Europhysics Lett.* **2023**, *142*, 34001. [CrossRef]
2. Lyu, T.; Dorenbos, P.; Wei, Z. Designing $LiTaO_3$:Ln^{3+},Eu^{3+} (Ln = Tb or Pr) Perovskite Dosimeter with Excellent Charge Carrier Storage Capacity and Stability for Anti-Counterfeiting and Flexible X-Ray Imaging. *Chem. Eng. J.* **2023**, *461*, 141685. [CrossRef]
3. Jacob, S.; Pandey, S.; Del Moral, J.; Karimzadeh, A.; Gil-Rostra, J.; González-Elipe, A.R.; Borrás, A.; Winkler, A. Surface Acoustic Waves Equip Materials with Active Deicing Functionality: Unraveled Deicing Mechanisms and Application to Centimeter Scale Transparent Surfaces. *Adv. Mater. Technol.* **2022**, 2300263. [CrossRef]
4. He, A.; Huang, H.; Zhou, L. Mechanical Properties and Deformation of $LiTaO_3$ Single Crystals Characterised by Nanoindentation and Nanoscratch. *Adv. Mater. Res.* **2012**, *565*, 564–569. [CrossRef]
5. Hang, W.; Zhou, L.; Zhang, K.; Shimizu, J.; Yuan, J. Study on Grinding of $LiTaO_3$ Wafer Using Effective Cooling and Electrolyte Solution. *Precis. Eng.* **2016**, *44*, 62–69. [CrossRef]
6. Li, Y.; Zhang, B.; Li, H.; Yang, X.; Wei, W.; Yang, Z. Analysis of Main Physical Factors of Chemical Mechanical Polishing About Lithium Tantalate. In Proceedings of the 2021 China Semiconductor Technology International Conference (CSTIC), Shanghai, China, 14–15 March 2021; pp. 8–10. [CrossRef]
7. Yuan, H.; Wei, X.; Du, H.W.; Hu, W.; Xiong, W. Influence of Polishing Parameters on Chemical Mechanical Polishing Processes of $LiTaO_3$ Wafer. *Key Eng. Mater.* **2006**, *315–316*, 561–565. [CrossRef]
8. Hang, W.; Huang, X.; Liu, M.; Ma, Y. On the Room-Temperature Creep Behavior and Its Correlation with Length Scale of a $LiTaO_3$ Single Crystal by Spherical Nanoindentation. *Materials* **2019**, *12*, 4213. [CrossRef]
9. Gruber, M.; Leitner, A.; Kiener, D.; Supancic, P.; Bermejo, R. Incipient Plasticity and Surface Damage in $LiTaO_3$ and $LiNbO_3$ Single Crystals. *Mater. Des.* **2018**, *153*, 221–231. [CrossRef]
10. Hang, W.; Zhou, L.B.; Shimizu, J.; Yuan, J.L. Study on Thermal Influence of Grinding Process on $LiTaO_3$. *Adv. Mater. Res.* **2013**, *797*, 252–257. [CrossRef]
11. Wei, X.; Yuan, H.; Du, H.W.; Xiong, W.; Huang, R.W. Study on Chemical Mechanical Polishing Mechanism of $LiTaO_3$ Wafer. *Key Eng. Mater.* **2006**, *304–305*, 310–314. [CrossRef]
12. Hang, W.; Wei, L.; Debela, T.T.; Chen, H.; Zhou, L.; Yuan, J.; Ma, Y. Crystallographic Orientation Effect on the Polishing Behavior of $LiTaO_3$ Single Crystal and Its Correlation with Strain Rate Sensitivity. *Ceram. Int.* **2022**, *48*, 7766–7777. [CrossRef]
13. Gao, S.; Kang, R.; Dong, Z.; Zhang, B. Edge Chipping of Silicon Wafers in Diamond Grinding. *Int. J. Mach. Tools Manuf.* **2013**, *64*, 31–37. [CrossRef]
14. Sun, J.; Qin, F.; Chen, P.; An, T.; Wang, Z. Edge Chipping of Silicon Wafers in Rotating Grinding. In Proceedings of the 2016 17th International Conference on Electronic Packaging Technology (ICEPT), Wuhan, China, 16–19 August 2016; pp. 1099–1103. [CrossRef]
15. Juri, A.Z.; Belli, R.; Lohbauer, U.; Ebendorff-Heidepriem, H.; Yin, L. Edge Chipping Damage in Lithium Silicate Glass-Ceramics Induced by Conventional and Ultrasonic Vibration-Assisted Diamond Machining. *Dent. Mater.* **2023**, *39*, 557–567. [CrossRef]
16. Hirobe, S.; Sato, Y.; Takato, Y.; Oguni, K. Numerical Analysis of Glass Edge Chipping by Impact Loading. *Int. J. Fract.* **2023**. [CrossRef]
17. Zhou, S.; Huang, X.; Lu, C.; Liu, Y.; Zhang, T.; Ma, Y. Revealing the Plastic Mode of Time-Dependent Deformation of a $LiTaO_3$ Single Crystal by Nanoindentation. *Micromachines* **2020**, *11*, 878. [CrossRef] [PubMed]
18. Ma, Y.; Huang, X.; Song, Y.; Hang, W.; Zhang, T. Room-Temperature Creep Behavior and Activation Volume of Dislocation Nucleation in a $LiTaO_3$. *Materials* **2019**, *12*, 1683. [CrossRef] [PubMed]
19. Park, Y.U. Surface Acoustic Wave Filter Theory. *Korean Inst. Electr. Electron. Mater. Eng.* **2000**, *13*, 8–13.
20. Guo, Y.J.; Zhang, J.; Zhao, C.; Ma, J.Y.; Pang, H.F.; Hu, P.A.; Placido, F.; Gibson, D.; Zu, X.T.; Zu, H.Y.; et al. Characterization and Humidity Sensing of ZnO/42° YX $LiTaO_3$ Love Wave Devices with ZnO Nanorods. *Mater. Res. Bull.* **2013**, *48*, 5058–5063. [CrossRef]
21. Varshni, Y.P. Temperature Dependence of the Elastic Constants. *Phys. Rev. B* **1970**, *2*, 3952–3958. [CrossRef]
22. Huo, Z.; Liu, T.; Li, T.; Wu, X.; Hu, J.; Zhang, X.; Zhong, H. A High Q and High Coupling SAW Resonator on Multilayer Polymide Substrate. In Proceedings of the 2021 IEEE International Conference on Advances in Electrical Engineering and Computer Applications (AEECA), Dalian, China, 27–28 August 2021; pp. 849–853. [CrossRef]
23. Kim, S.W.; Jeong, Y.J.; Lee, H.C. Effects of the Mixing Method and Sintering Temperature on the Characteristics of PZNN-PZT Piezoelectric Ceramic Materials. *J. Korean Powder Met. Inst.* **2018**, *25*, 487–493. [CrossRef]
24. Guber, M.; Kraleva, I.; Supancic, P.; Bielen, J.; Kiener, D.; Bermejo, R. Strength Distribution and Fracture Analyses of $LiNbO_3$ and $LiTaO_3$ Single Crystals under Biaxial Loading. *J. Eur. Ceram. Soc.* **2017**, *37*, 4397–4406. [CrossRef]

25. Li, J.; Zhou, X.; Zhu, W.; Li, J.; Jing, F. A Shock-Induced Phase Transformation in a $LiTaO_3$ Crystal. *J. Appl. Phys.* **2007**, *102*, 083503. [CrossRef]
26. Wort, C.J.H.; Balmer, R.S. Diamond as an Electronic Material. *Mater. Today* **2008**, *11*, 22–28. [CrossRef]
27. Spear, K.E.; Dismukes, J.P. (Eds.) *Synthetic Diamond: Emerging CVD Science and Technology*, 25th ed.; John Wiley & Sons: New York, NY, USA, 1994.
28. Julean, D. SPH Simulation of Single Grain Action in Grinding. *MATEC Web Conf.* **2017**, *137*. [CrossRef]
29. Shi, D.; Hou, Q.; Ma, T.; Zhao, T.; Pan, J. Analysis of the High-Efficiency and Low-Damage Abrasive Processing Mechanism for SiC Based on the SPH Simulation of Single-Grain Indentation and Scratching. *AIP Adv.* **2022**, *12*, 055001. [CrossRef]
30. Mosavat, M.; Rahimi, A. Numerical-Experimental Study on Polishing of Silicon Wafer Using Magnetic Abrasive Finishing Process. *Wear* **2019**, *424–425*, 143–150. [CrossRef]
31. Khodaii, J.; Adibi, H.; Barazandeh, F.; Solhtalab, A.; Rezaei, M.; Sarhan, A.A.D. Improvement of Surface Integrity in the Grinding of Bioceramic Partially Stabilized Zirconia Using Analytical, Numerical, and Experimental Methods. *Ceram. Int.* **2020**, *46*, 13784–13797. [CrossRef]

Disclaimer/Publisher's Note: The statements, opinions and data contained in all publications are solely those of the individual author(s) and contributor(s) and not of MDPI and/or the editor(s). MDPI and/or the editor(s) disclaim responsibility for any injury to people or property resulting from any ideas, methods, instructions or products referred to in the content.